Nanoscale Advances

ROYAL SOCIETY OF CHEMISTRY

PAPER

View Article Online
View Journal | View Issue

Cite this: *Nanoscale Adv.*, 2025, **7**, 2608

Mangrove pneumatophores as biocatalysts for the fabrication of silver nanoparticles and their potential applications against biofilm formation and hepatic carcinoma

Debasis Nayak, †[a] Awdhesh Kumar Mishra,†[b] Kunal Biswas,[c] Asmita Sen,[a] Chandana Malakar,[d] Jibanjyoti Panda,[a] Neelam Amit Kungwani,[e] Sarvesh Rustagi,[f] Bibhu Prasad Panda *[g] and Yugal Kishore Mohanta *[hi]

The current study demonstrates the biogenic synthesis of silver nanoparticles using the pneumatophores of *Acanthus ilicifolius* (AiP-AgNPs), which is cost-effective and biocompatible. *A. ilicifolius* possesses remarkable features to endure the harshest conditions for its entire life cycle and generates secondary metabolites for its sustainability in hostile mangrove ecosystems. The presence of a prominent UV-visible absorption band at 420 nm supported the distinct color change inference for the synthesized AiP-AgNPs. The size of the synthesized AiP-AgNPs was determined to be ~15 nm through field emission-scanning electron microscopy (FE-SEM), transmission electron microscopy (cryo-TEM), and atomic force microscopy (AFM). The presence of secondary metabolites such as 2-bromo-1,1-dichloroethene, hemin and *N*-(sulfanylacetyl)-L-seryl-L-argininamide was indicated by prominent peaks in liquid chromatography, suggesting their probable roles in the synthesis of AgNPs. The synthesized AiP-AgNPs demonstrated a distinct zone of inhibition against *Pseudomonas aeruginosa* (15.33 mm), *Vibrio cholerae* (9.83 mm), and *Bacillus subtilis* (12 mm). They also exhibited concentration-dependent antioxidant activity in DPPH, nitric oxide, and hydrogen peroxide scavenging assays. The anticancer potential of the synthesized AiP-AgNPs against HepG2 hepatocarcinoma cells determined through MTT colorimetric assay and flow cytometry revealed their dose-dependent cytotoxicity with the occurrence of the sub-G_0 phase (25.6%). Subsequent analysis using fluorescence microscopy, DNA damage, comet assay, and migration assay indicated that AiP-AgNPs hold significant potential and the ability to serve as a therapeutic candidate to pave the way for further in-depth investigations for pre-clinical and clinical research purposes.

Received 30th August 2024
Accepted 3rd March 2025

DOI: 10.1039/d4na00722k

rsc.li/nanoscale-advances

1. Introduction

Biomedical and pharmaceutical studies delve deeply into exploring novel biomasses or components that can aid in developing biologically active therapeutics that can significantly reduce the global mortality rate.[1–4] Nanoscience and nanotechnology are the most popular tools that have emerged recently, and they have found their applicability in every field of modern

[a]*Bioresources and Traditional Knowledge Laboratory, Department of Wildlife and Biodiversity Conservation, Maharaja Sriram Chandra Bhanja Deo University, Sriram Chandra Vihar, Takatpur, Baripada, Mayurbhanj, Odisha, 757003, India. E-mail: deb63nayak@gmail.com; asmitasen872@gmail.com; jibanjyotipanda83@gmail.com*

[b]*Department of Biotechnology, Yeungnam University, Gyeongsan 38541, Gyeongsangbuk-do, Republic of Korea. E-mail: awadhesh.biotech07@gmail.com*

[c]*Centre for Nanoscience & Nanotechnology International Research Centre, Sathyabama Institute of Science and Technology, Jeppiaar Nagar, Rajiv Gandhi Salai, Chennai 600119, India. E-mail: kunalbiswas.irc@sathyabama.ac.in*

[d]*Environmental Biotechnology Laboratory, Life Science Division, Institute of Advanced Study in Science and Technology, Paschim Boragaon, Guwahati-781035, Assam, India. E-mail: chandanamalakar63@gmail.com*

[e]*Marine Biotechnology, Gujarat Biotechnology University, Gandhinagar 382355, India. E-mail: neelam.kungwani@gbu.edu.in*

[f]*Department of Food Technology, Uttaranchal University, Dehradun, Uttarakhand, 248007, India. E-mail: sarveshrustagi@gmail.com*

[g]*Environmental Sciences, Department of Chemistry, ITER, Siksha 'O' Anusandhan (Deemed to be University), Bhubaneswar, Odisha, 751030, India. E-mail: bibhuprasadpanda@soa.ac.in*

[h]*Nano-biotechnology and Translational Knowledge Laboratory, Department of Applied Biology, School of Biological Sciences, University of Science and Technology Meghalaya, Techno City, 9th Mile, Baridua, Ri-Bhoi-793101, Meghalaya, India. E-mail: ykmohanta@gmail.com*

[i]*Centre for Herbal Pharmacology and Environmental Sustainability, Chettinad Hospital and Research Institute, Chettinad Academy of Research and Education, Kelambakkam-603103, Tamil Nadu, India*

† Authors contributed equally to this work and are treated as joint first authors.

lifestyle.[5–7] Nanoparticles are particles with dimensions on the nanometre scale and possess a variety of features that make them suitable candidates in several industries including textiles, materials science, electronics, and healthcare.[8,9] Numerous methodologies have been employed to synthesize cost-effective nanoparticles with negligible toxicity to cap bioactive compounds for targeted delivery.[10–13]

Mangroves are unique and resilient coastal ecosystems well known for their remarkable adaptability to challenging intertidal zones. Their intricate web of life with distinct survival mechanisms in response to abiotic and biotic stress has fascinated researchers to elucidate their ecological and biological properties.[14,15] Traditional healers and native people have exploited the mangroves for millennia to comprehend their medicinal and therapeutic potential.[16] Various research groups have demonstrated that mangroves possess significant amount of polyphenols and secondary metabolites in order to adapt to their adverse environmental conditions.[17] These biologically active compounds could be isolated and processed in the pharmaceutical and nutraceutical industries.[18,19] The most striking feature of mangroves is their pneumatophores, which are their specialized roots that serve as a crucial link for their survival in waterlogged, saline, and oxygen-derived soils.[20] Pneumatophores possess many phytochemicals (a botanical reference material (BRM)), such as phenols, flavonoids, saponins, tannins, triterpenoids, alkaloids, glycosides, steroids, anthraquinones, coumarins and essential oils.[21–23] Hence, pneumatophores have been actively screened by various research groups[24,25] owing to their antioxidant, antidiabetic, anti-inflammatory and anticancer properties, thereby endorsing their potential use in the medical, agricultural and biotechnological fields.

Acanthus ilicifolius, a significant mangrove plant, has prickly edges and resembles sea holly leaves. It belongs to the Acanthaceae family and is found in India's East and West coasts, Meghalaya, and Andaman Islands.[26] These plants are known for their antibacterial activities owing to the diverse and ever-rising content of bioactive chemicals.[27] In traditional medicine such as ayurveda, *A. ilicifolius* has been prescribed as an aphrodisiac, blood-purifier, purgative agent, pain reliever, leucorrhoea decoctions, antipyretic, muscle relaxant, hypnotic, diuretic and snake bite.[28,29] Various active compounds, such as 2-benzoxazoline, benzoxazinium, ursodeoxycholic acid, 9,19-cyclolanostan-3-ol, 24-methylene-, (3a′), trilostane, 21-hydroxyprogesterone and trifluoroacetate, have demonstrated strong potential as antiviral, antifungal, anticancer, antibacterial, and anti-insecticidal properties.[30,31]

The eastern coast of India, specifically the state of Odisha, has a vast coastal line of about 480 km long; hence, it provides unique biodiversity to the coastal region of Odisha. The pneumatophores of mangrove plants protect coastal regions from sea erosion and provide many therapeutic potentials to the people residing in the coastal regions. Pneumatophores are excellent biocatalysts showing the remarkable adaptability of mangrove plants and demonstrating how harnessing nature's ingenuity can lead to sustainable solutions that benefit to both our society and the environment. The development of modern use for pneumatophores outside of their biological functions is possible in the field of nanotechnology. However, pneumatophores have not been exploited regarding their efficacy in synthesizing nanoparticles and their therapeutic potential. Owing to relative abundance around the coastal regions of Odisha along with their giant potential in biomedical applications, the pneumatophores of *Acanthus ilicifolius* were exploited due to their bioengineering potential to synthesize novel AgNPs with their application in HepG2 hepatocarcinoma cancerous cells.

2. Methodology

3-(4,5-Dimethylthiazol-2-yl)-2,5-di-phenyl-tetrazolium bromide (MTT), Dulbecco's modified Eagle's medium (DMEM), fetal bovine serum (FBS), antibiotic solution (penicillin–streptomycin), dichloro-dihydro-fluorescein diacetate (DCHF-DA), rhodamine 123, and propidium iodide were purchased from Sigma-Aldrich (Mumbai, India). Silver nitrate, nutrient agar and nutrient broth, agarose, 100 bp DNA ladder and all other reagents of analytical grade were purchased from Hi-Media (Mumbai, India). Distilled water was used throughout the experiments.

2.1. Preparation of the pneumatophore extract

The *Acanthus ilicifolius* pneumatophores were collected from the Kasturikana locality in the Bhadrak district of Odisha, India (latitude 20.76386°; longitude 86.816779°). The collected specimens were identified in the Department of Botany, University of Science and Technology, Meghalaya. The pneumatophores were cleaned, dried, and powdered using a mortar and pestle. For the extract preparation in a 500 mL conical flask, 20 g of powdered samples were weighed and vortexed with 200 mL of distilled H_2O using a magnetic hot stirrer for 2 hours at 50 °C. After incubation, the final solution was filtered and stored at 4 °C for further use.

2.2. Phytochemical analysis of *A. ilicifolius* pneumatophores

The pneumatophore extract was subjected to Liquid Chromatography-High Resolution Mass Spectrometry (LC-HRMS) analysis using Orbitrap Exploris 240 Mass Spectrometer with Hypersil Gold 5UM-250X4 6 mm column (Thermo Fisher). For metabolic separation, two binary mobile phases comprising two solutions (solution A containing water with 0.1% formic acid and solution B containing acetonitrile with 0.5% formic acid) were used. Operating at a flow rate of 0.3 mL min^{-1}, with a 10 μL injection volume, HRMS was conducted in full MS/dd-MS2 mode across m/z 100–1500 in both positive and negative ion modes.[32]

2.3. Synthesis of silver nanoparticles

90 mL of $AgNO_3$ salt solution (0.1 M) and 10 mL of *Acanthus ilicifolius* pneumatophore extract were mixed in a 9 : 1 ratio in a volumetric flask. Using a magnetic hot plate, the precursor salt and extract concoction were incubated at 80 °C and 200 rpm for 90 minutes. After the initial color changed to dark brownish

red, the resultant solution was washed three times in distilled water by centrifugation (C24-BL centrifuge, REMI, India) at 10 000 rpm for 30 min each. After decanting the supernatant aqueous layer, the resulting pellet was gathered, lyophilized, and kept for subsequent analysis at an ambient temperature.[33,34]

2.4. Characterization of synthesized nanoparticles

The as-prepared samples of *Acanthus ilicifolius* pneumatophore-mediated silver nanoparticles (AiP-AgNPs) were dissolved in distilled water and sonicated for 30 min. The diluted AiP-AgNPs were subjected to UV-Vis spectroscopy (Lambda 35® (PerkinElmer, Waltham, MS, USA)). The hydrodynamic size (*Z*-average diameter), surface zeta potential (surface charge), and poly disparity index (PDI) of the synthesized nanoparticles were characterized through dynamic light scattering measurements (ZS 90, Malvern Instruments Ltd, Malvern, UK). The AiP-AgNPs were sonicated, and the diluted samples were scanned to ascertain their surface colloidal stabilities. The surface morphology of the synthesized nanoparticles was observed through cryo-transmission electron microscopy (cryo-TEM) with EDAX. The AiP-AgNPs were subjected to carbon-coated copper grids of mesh size 300 and were measured using cryo-TEM instrumentation (cryo-TEM) (Tecnai™ F30 G2 STWIN, FEI, USA) at 200 kV. The obtained images were plotted at 20 nm scale bar magnification. The as-synthesized powder of AiP-AgNPs was further exposed to field emission-scanning electron microscopy (FE-SEM) (Nova NanoSEM 450/FEI, USA) to ascertain the particle size. The powder samples were coated with gold sputter under a vacuum, and its surface topography was obtained at a 500 nm scale bar operating at 15 kV voltage. The synthesized AiP-AgNPs were further characterized through atomic force microscopy (AFM) (Dimension D3100, Veeco). The sonicated AiP-AgNPs were drop cast in glass coverslips, dried, and exposed to AFM with a conducting P (n)-doped silicon tip under normal atmospheric conditions in non-tapping mode. The resulting images were analyzed in 2D and 3D forms along with the height profile to uncover the thickness profile of the synthesized AiP-AgNPs. The synthesized powder samples of AiP-AgNPs were subjected to X-ray diffraction (XRD) measurements (PANalytical X'Pert, Almelo, The Netherlands) using a Ni filter and a Cu Kα (l = 1.54056 Å) radiation source. The diffraction angles ranged from 20 to 80 degrees, while the rate of scanning was captured at 0.05 degrees. The obtained diffractogram was plotted in the intensity (a.u.) *versus* 2θ (in degrees), and the different crystalline lattice planes were plotted and corroborated with previous studies for the verification and formation of AgNP peaks. The functional groups in the pneumatophore-mediated AgNPs were scanned using Fourier-transform infrared spectroscopy (FTIR) (Shimadzu 8400S). With an average of 25 scans per sample, the scanning range was 4000–500 cm^{-1}. Origin software was used to evaluate the results. The thermo-gravimetric analysis (TGA) of the synthesized AiP-AgNPs was conducted to measure their thermal stability. A 15 g of the lyophilized AiP-AgNP powder samples were exposed to different temperature ranges from 200 to 800 °C, and the % weight loss as a function of the imparted temperature was measured. The loss of different volatile components and molecules with lower melting temperatures occurred, and the residual weight percentage of mass (mg) was calculated and analyzed for the thermal and gravimetric parameters associated with the different physicochemical properties of the nanomaterial.

2.5. Antioxidant activity

2.5.1. DPPH scavenging assay. The synthesized AiP-AgNPs and the pneumatophore aqueous extract were screened for their DPPH radical scavenging activity.[35] The DPPH stock (4 mg/100 mL methanol) solution was prepared, and accordingly, 1 mL of the DPPH solution was added to 1 mL of AiP-AgNPs and mangrove pneumatophore extract in various concentrations (10–100 μg mL^{-1}). The reaction mixture was incubated for 30 min, and the absorbance was measured spectrophotometrically at 517 nm. Ascorbic acid was used as the positive control.

2.5.2. Hydrogen peroxide scavenging activity. A standard methodology was employed to assess the hydrogen peroxide (H_2O_2) scavenging activity of the manufactured AiP-AgNPs and pneumatophore aqueous extract.[36] 40 mM of H_2O_2 was dissolved in PBS (phosphate buffer saline; pH 7.4). 2.5 mL of PBS, 0.6 mL of H_2O_2, and 100 μg mL^{-1} of AiP-AgNPs and pneumatophore aqueous extract were added. After 30 min of incubation, the absorbance was measured at 230 nm. The control solution contained only H_2O_2 and PBS.

2.5.3. Nitric oxide (NO) scavenging activity. The NO scavenging activity of the synthesized nanoparticles and pneumatophore aqueous extract was determined following standard protocol.[37] Briefly, in a test tube, different concentrations (10–100 μg mL^{-1}) of the AiP-AgNPs and pneumatophore aqueous extracts were taken, followed by the addition of $Na_2[Fe(CN)_5NO]$ (1 mL), and the combination was incubated at 25 °C for 150 min. Then, 1 mL of the solution was pipetted to another test tube, and 1 mL of Griess reagent was added. The absorbance of the reaction solution was recorded at 546 nm after 30 min.

2.6. Screening the hemocompatibility of synthesized AiP-AgNPs

2.6.1. Hemolysis assay. The biocompatibility of AiP-AgNPs and pneumatophore aqueous extract with the red blood corpuscles was determined.[38] Briefly, goat blood was collected from a local butcher shop near Takatpur Market, Baripada, Odisha, India. The collected sample was centrifuged, and the obtained RBC pellets were diluted with PBS (pH 7.4) and kept for further experimental work. The diluted blood was combined in a 1 : 9 ratio with normal saline for the hemolysis assay. 1 mL of pneumatophore aqueous extract (1 mg L^{-1} concentration) and manufactured AiP-AgNPs were combined with 5 mL of diluted blood in a 15 mL Eppendorf tube. The resulting solution was then incubated at 37 °C for 30 min. Following the incubation period, the reaction mixture was centrifuged for 10 min at 3000 rpm to determine the OD of the supernatant at 540 nm.

2.6.2. Hemagglutination assay. Similarly, for the hemagglutination assay, in a 96 well round bottom plate 200 μL of diluted blood prepared in the hemolysis assay was added to

each well, followed by serial dilution of 100 μL of the synthesized AiP-AgNPs and pneumatophore aqueous extract in all wells except the last two rows (11th and 12th), which were designated as negative and positive controls, respectively. After 60 min of incubation at 37 °C, the wells were observed for the formation of round button-like structures at the bottom.

2.7. Antibacterial activity

The pneumatophore aqueous extract and manufactured AiP-AgNPs were tested using the bacterial strains of *Pseudomonas aeruginosa* (MTCC No. 424), *Vibrio cholerae* (MTCC No. 15025), and *Bacillus subtilis* (MTCC No. 441) obtained from NCCS Pune, India, using the agar well diffusion antibacterial assay. 20 mL of sterilized nutrient broth (Hi-Media Labs, Mumbai) was used to inoculate the bacterial strains in an inoculating flask, and the flask was then incubated for 24 h at 37 °C. The bacterial strains were speared onto previously prepared agar plates, which were further processed with 200 μL wells using a sterile cork borer. Finally, each well received 100 μL of the test sample sonicated aqueous solution, which was then incubated for 24 h at 37 °C. The zone of inhibition against each bacterial strain was measured to observe the antibacterial activity.

2.8. Anti-biofilm activity

2.8.1. Tube assay. The anti-biofilm potential of the synthesized AiP-AgNPs and pneumatophore aqueous extract against the *P. aeruginosa* bacteria was determined using a standard protocol.[39] To screen for biofilm-inhibiting activity, *P. aeruginosa* was used because it is well reported for forming biofilm.[40] For the tube assay, the *P. aeruginosa* was inoculated at 10^{-3} in Nutrient broth, followed by the addition of 100 μL of AiP-AgNPs and pneumatophore aqueous extract. After 7 days of incubation, the test tubes were rinsed and fixed with sodium acetate before the addition of 0.1% crystal violet solution. The test tubes were observed for possible ring formation; subsequently, the OD was measured at 620 nm to observe their % biofilm inhibition activity.

2.8.2. Congo red assay. For the Congo red assay, brain heart infusion (BHI) agar (37 g) and sucrose (50 g) were dissolved in distilled water (800 mL), and Congo red (0.8 g) was autoclaved separately. When the BHI agar was cooled to 50 °C, the autoclaved Congo red solution was added and poured into previously sterilized Petri plates. The previously incubated bacteria with the AiP-AgNPs and pneumatophore aqueous extract were streaked onto solidified BHI–Congo red agar plates and incubated at 37 °C. The formation of black colonies specified strong biofilm-forming activity, and the occurrence of red colonies was considered a non-biofilm-forming activity.[41]

2.9. MTT assay

The % cell viability and toxicity of AiP-AgNPs were determined using the MTT assay, following a standard protocol with required modifications.[42] Briefly, HepG2 hepatocarcinoma cells (NCCS, Pune, India) were grown in a 96 well plate using a Dulbecco's modified Eagle's medium (DMEM) supplemented with fetal bovine serum (FBS) and 1% antibiotic solution. After 70% confluency, the media was discarded, and different concentrations (10–200 μg mL^{-1}) of AiP-AgNPs were incubated with HepG2 cells for 24 h at 37 °C in a CO_2 incubator. Later, 100 μL of MTT (5 mg mL^{-1}) was added, and the plate was incubated for 4 h. After discarding the MTT solution, 100 μL of DMSO was pipetted and incubated for 15 min under dark conditions. Finally, the OD was scanned at 595 nm using a plate reader (2030 Multilabel Processor Victor™X3, PerkinElmer, USA).

2.10. Cell cycle analysis by flow cytometer

The effect of the AiP-AgNPs on the cell cycle of HepG2 hepatocellular carcinoma cells was analyzed by applying a BD Accuri C6 flow cytometer (BD Biosciences).[43] Briefly, the HepG2 cells were grown in a 6 well plate, and after 70% confluency, the cells were harvested by trypsinization. The obtained cells were further incubated with AiP-AgNPs for 24 hours in a CO_2 incubator. After incubation, the cells were trypsinized and treated with propidium iodide (PI) dye and kept at 4 °C for 30 min before flow cytometry (B6 Accuri, BD Biosciences).

2.11. Chromatin condensation assay by Hoechst 33342 staining

Following standard protocol,[44] the Hoechst 33342 staining was performed on HepG2 hepatocellular carcinoma cells upon treatment with AiP-AgNPs. Briefly, the HepG2 carcinoma cells were grown with the synthesized AiP-AgNPs for 12 h. Subsequently, the media was discarded, and the cells were rinsed, followed by the addition of Hoechst 33342 (1 mg mL^{-1}). After 10 min of incubation, the cells were observed for condensed chromatin using epifluorescent microscopy under a UV filter (Olympus IX71, Olympus, Tokyo, Japan).

2.12. DNA fragmentation and comet assay

The interaction between the DNA of HepG2 hepatocarcinoma cells and the synthesized AiP-AgNPs was demonstrated to assess the DNA impairment caused by the incubation of the HepG2 cells with AiP-AgNPs.[44] Briefly, HepG2 cells were grown overnight with AiP-AgNPs. After incubation, the HepG2 cells were collected, and the DNA was isolated using the DMSO method.[42] The fragmented DNA bands were scrutinized using a gel-documentation system (Bio-Rad, India). A comet assay was executed to detect the amelioration of DNA in individual cell stages. The AiP-AgNP-treated HepG2 hepatocarcinoma cells were collected and treated with low-melting agarose, followed by gel electrophoresis in glass slides. The low-melting agarose-containing slides were then treated with PI dye, and images were captured using an epifluorescent microscope. Various parameters associated with the comet were analyzed using ImageJ OpenComet.

2.13. Detection of total internal ROS production

The total internal ROS production of the AiP-AgNPs against HepG2 hepatocarcinoma cells was evaluated by the dichlorodihydro-fluorescein diacetate (DCFH-DA) staining. Briefly, the HepG2 hepatocarcinoma cells were grown in a 60 mm Petri

plate, and AiP-AgNPs were subsequently added. After incubation for 12 h, DCFH-DA dye was added, and the cells were further kept for 4 h before examination through flow cytometry.

2.14. Migration assay

The migration assay of the HepG2-treated cells with the AiP-AgNPs was conducted to study the migration of the hepatocellular carcinoma cells following standard protocol.[44] Briefly, the HepG2 carcinoma cells were seeded into 20 mm Petri plates, and using a sterile micro tip, a line was stretched. The media was discarded, and fresh media containing AiP-AgNPs was added to the wells. Pictures were taken using a phase contrast bright field microscope (Olympus) at regular time intervals (0^{th} h and 24^{th} h of incubation).

2.15. Statistical analysis

The Duncan test was used to assess the statistical significance of the data. The presentation of all the data are in mean ± standard deviation (SD). At $p < 0.05$, the data were deemed statistically significant. Each experiment was run in triplicate.

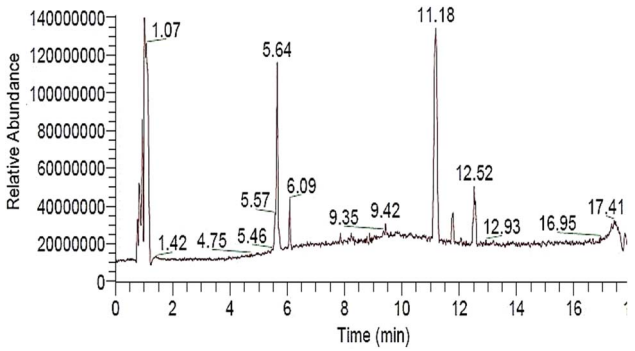

Fig. 1 Liquid chromatography-high resolution mass spectrometry (LC-HRMS) chromatogram of *A. ilicifolius* pneumatophores extract.

3. Results and discussion

Peaks were identified in liquid chromatography with tandem mass spectrometry chromatograms with the assistance of an accessible *m*/*z* database (Mass Bank of Europe and National Library of Medicine) and a literature survey (Fig. 1). Because secondary metabolites can also occur in isomeric forms (aglycones) or isobaric compounds, the experimental chromatograms are cited as tentative. Moreover, acylating groups may coexist in different configurations with sugar moieties. The preceding tabulation does not include the components that are present in small amounts (Table 1). Major compounds were detected with sharp peaks, such as L-β-(3-hydroxyureido)-alanine, *N*-hexadecyl-ethanolamine, Fluo-5F, 2-bromo-1,1-dichloroethene, hemin, *N*-(sulfanylacetyl)-L-seryl-L-argininamide, myristyl sulfate, iodothiophene, di(2-ethylhexyl) phthalate, and naphthacemycin C1.

Protein synthesis requires the essential amino acid alanine, where tryptophan and vitamin B-6 metabolize, and they assist as fuel for muscles and the central nervous system. It enhances the immune system and facilitates the body's utilization of carbohydrates. Ethanolamine is a transparent, viscous substance that can exist as a liquid or solid below 51 °F (10.5 °C). It has a gentle odor resembling that of ammonia. Manufacturers use sodium hydroxide to produce soap, detergents, ink, colors, and rubber. Myristyl sulfate is a blend of chemical molecules that possess the characteristics of both detergents and surfactants. It is present in numerous personal care items, including soaps, shampoos, and toothpaste. Hemin, an injectable iron-containing medication, alleviates recurring episodes of acute intermittent porphyria (AIP) during the menstrual cycle when carbohydrate treatment is ineffective.

Table 1 Phytochemicals present in the *A. ilicifolius* pneumatophore extract characterized using LC-HRMS

RT	Formula	Compound	Avg. MW
7.01	$C_{25}H_{35}NO_6$	Neopestalotin D	445.24645
7.33	$C_4H_9N_3O_4$	L-β-(3-Hydroxyureido)-alanine	163.05892
8.93	$C_{18}H_{37}NO_2$	*N*-Hexadecyl-ethanolamine	299.28225
9.85	$C_{22}H_{43}NO_3$	Semiplenamide F	369.3243
11.49	$C_{22}H_{43}NO$	Erucamide	337.3344
16.11	$C_{32}H_{29}ClO_9$	Naphthacemycin C1	592.14953
1.00	$C_{35}H_{27}F_3N_2O_{13}$	Fluo-5F	740.14421
1.07	C_2HBrCl_2	2-Bromo-1,1-dichloroethene	173.86312
5.64	$C_{34}H_{32}ClFeN_4O_4$	Hemin	651.14792
9.42	$C_{18}H_{25}NO_2S_2$	*N*-[5-(1,3-Dithian-2-yl)-2-pentyn-1-yl]-3,4-dimethoxy-*N*-methylaniline	351.13261
11.18	$C_{11}H_{22}N_6O_4S$	*N*-(Sulfanyl acetyl)-L-seryl-L-argininamide	334.14268
12.52	$C_{14}H_{30}O_4S$	Myristyl sulfate	294.18645
12.52	$C_{26}H_{50}N_3O_7P$	3-[(13-Methyltetradecyl)oxy]propyl hydrogen ({[(2*S*)-1-(4-amino-2-oxo-1(2*H*)-pyrimidinyl)-3-hydroxy-2-propanyl]oxy}methyl)phosphonate	547.33934
m/z			
288.9216	C_4H_3IS	Iodothiophene	209.8994
391.2844	$C_{24}H_{38}O_4$	Di(2-ethylhexyl)phthalate	390.27711
610.1841	$C_{32}H_{29}ClO_9$	Naphthacemycin C1	592.14953
684.2033	$C_{32}H_{41}Cl_4N_5O_3$	3,5-Dichloro-*N*-[(2*Z*,3*R*)-3-(3,4-dichlorophenyl)-5-[4-(3-isopropyl-2-oxotetrahydro-1(2*H*)-pyrimidinyl)-1-piperidinyl]-2-(methoxyimino)pentyl]-*N*-methylbenzamide	683.19475

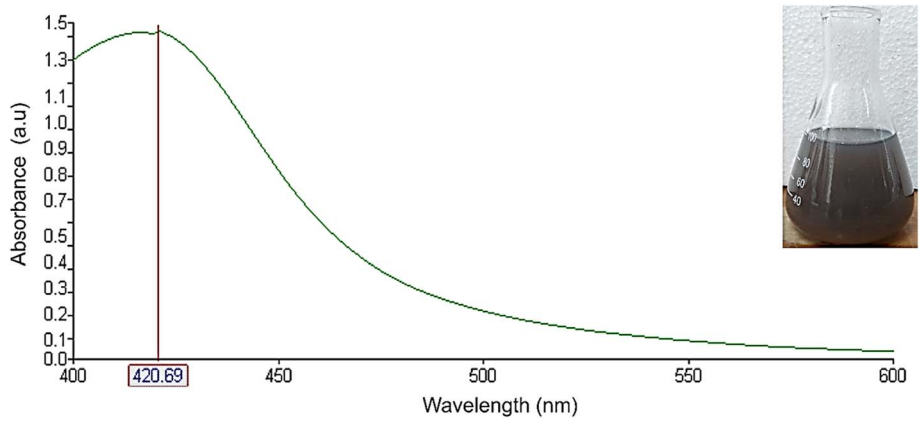

Fig. 2 UV-visible spectrum of the synthesized AiP-AgNPs, and their colour change inference (inset) confirming the visual observation for the synthesis of AgNPs.

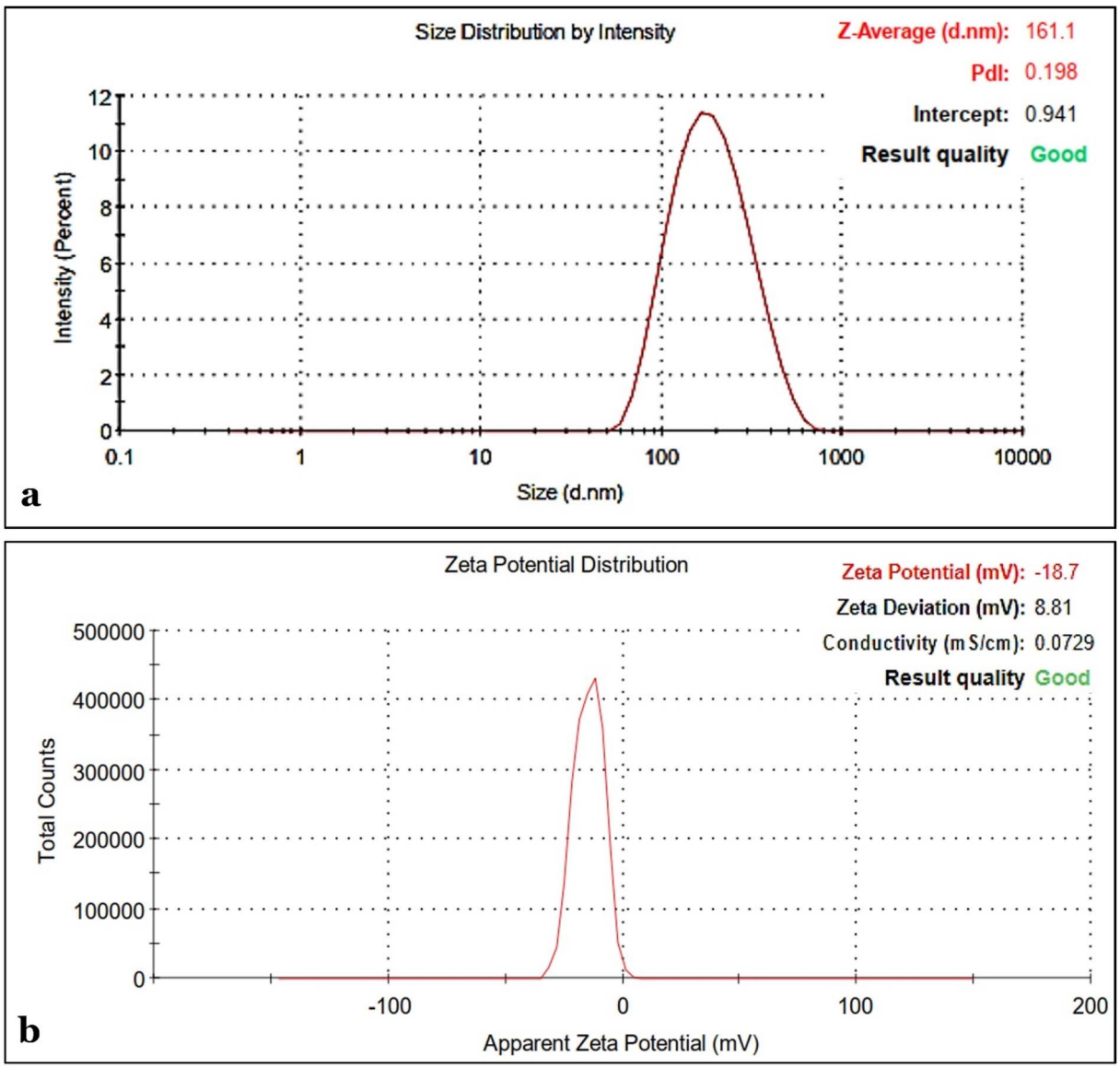

Fig. 3 Dynamic light scattering measurements of the synthesized AiP-AgNPs: (a) hydrodynamic size (*Z*-average diameter) and (b) surface charge (zeta potential).

When added to imipenem at a concentration of 0.5 μg mL^{-1}, naphthacemycins made it 100–500 times more effective against methicillin-resistant *Staphylococcus aureus* (MRSA).[45]

UV-Vis spectroscopy is a technique in which the absorbance of the sample is measured at a particular wavelength.[46] The sample of the UV-Vis spectroscopy exhibits an absorbance of ~420 nm, which is a reflection of the Surface Plasmon Resonance (SPR) at the surface of the silver nanoparticles. It is understood that owing to the larger number of surface electrons at the surface of the AgNPs, there is an occurrence of quantization at the electronic level, which results in the production of such characteristic absorbance at 420 nm, indicating a clear formation of AgNPs by the pneumatophore extract of *Acanthus ilicifolius* (Fig. 2).

Fig. 3 shows the hydrodynamic diameter and surface charge distribution of the as-synthesized AiP-AgNPs using Dynamic Light Scattering (DLS) measurements. The size distribution pattern of the as-synthesized AiP-AgNPs in their colloidal state

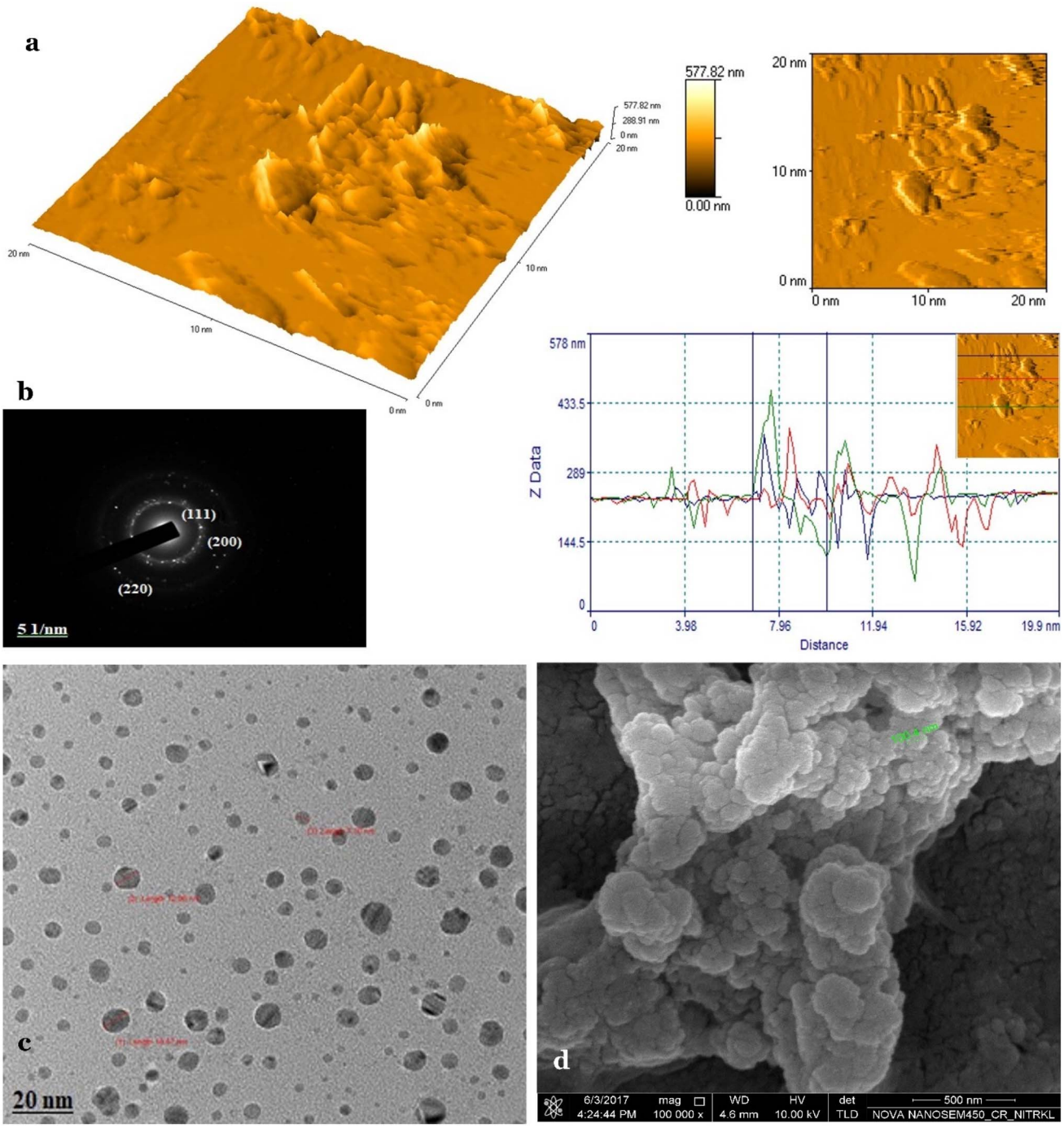

Fig. 4 Visualization of surface morphology and texture analysis using (a) atomic force microscopy; (b) selected area electron diffraction using cryo-TEM; (c) cryo-transmission electron microscopy; and (d) field emission-scanning electron microscopy image at 100 000× magnification.

was calculated to be around ~161 d nm with a PDI value of 0.198, confirming their mono-disperse nature. Their surface zeta potential was observed to be ~−18.7 mV, indicating its good colloidal stability.

The surface morphology and topography of the synthesized AiP-AgNPs were visualized using electron microscopy (AFM, cryo-TEM, and FE-SEM). The AFM is used for measuring the available forces taking place between the AFM tip and the sample surface.[47] The different surface properties, such as surface roughness, corrugation, and differential charge distribution, are evident in Fig. 4a. The thickness of the synthesized AiP-AgNPs was ~12 nm, as evident from the height profile of the AFM studies. The net charge distribution owing to the bottom-up synthesis of AiP-AgNPs from the green route-mediated synthesis was also evident from the differential colour distribution in the 3D image of AFM. It is evident from Fig. 4c that poly-disperse AiP-AgNPs are formed in the as-synthesized biogenic formation of AgNPs. The cryo-TEM micrograph demonstrates the formation of spherical AgNPs when tested in cryo-TEM at 200 kV. The as-synthesized AiP-AgNPs were of regular shape and had an average dimension size of ~15 nm. The clear concentric rings in the SAED pattern indicate poly-crystallinity in the as-synthesised nanoparticles. Different dots in the concentric rings indicate different lattice planes of the crystalline AgNPs, as shown in Fig. 4b. Further, the surface morphology of the AiP-AgNPs was measured using FE-SEM analyses. The different structures and sizes of the nanomaterials are observed from FE-SEM micrographs. ~165–180 nm poly-dispersed sizes of the AgNPs were synthesized using the pneumatophore aqueous extract of *A. ilicifolius* (Fig. 4d). The majority of the nanoparticles from the topical view are spherical, with few among them being irregular. The different structures of the nanomaterials are the result of the green route-mediated reduction of the precursor molecules, such as $AgNO_3$, and different phyto-compounds associated with the bottom-up synthesis of AgNPs.

It is evident from Fig. 5 that the AiP-AgNPs synthesized from the pneumatophore aqueous extract exhibit numerous elemental groups in their native structure. Prominent silver (Ag) peaks were observed in good numbers in the EDAX profile. The formation of AiP-AgNPs from different precursor molecules, such as $AgNO_3$, and associated functional groups, such as ketones, alcohol groups (–OH), and carboxylic acid groups (–COOH), resulted in the synthesis of AiP-AgNPs. The ionic state conversions from Ag^{2+} to Ag^0 in the reduction procedure of the synthesis of AgNPs lead to the formation of several Ag peaks in the EDAX profile. The EDAX studies support the morphological observation of the AgNPs[48] in the cryo-TEM studies, in which the as-synthesized spherical AiP-AgNPs, as evident from cryo-TEM studies, corroborate the respective elemental peaks in the EDAX studies. The additional Cu and C peaks observed are from the carbon-coated copper grids used for sample holding during slide preparation under cryo-TEM characterizations.

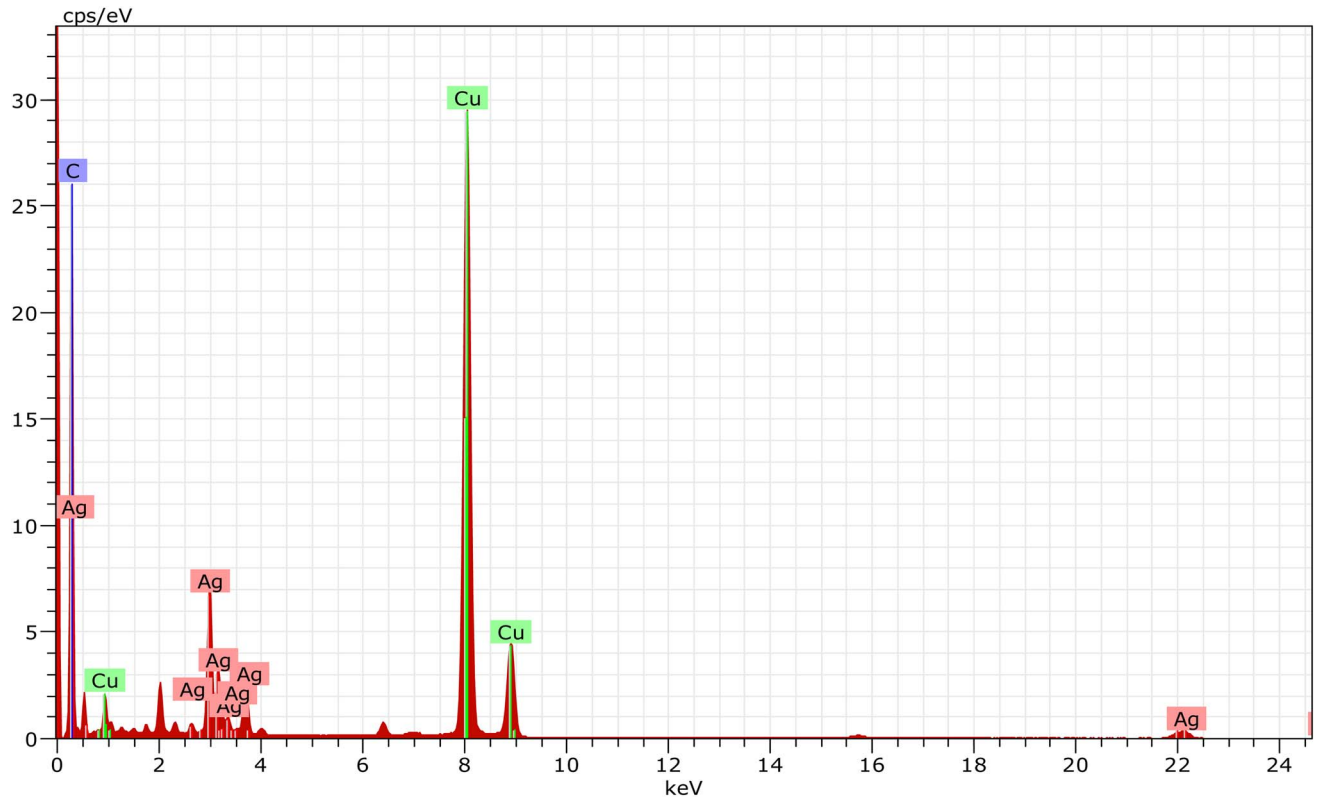

Fig. 5 Energy-dispersive X-ray spectroscopy (EDAX) of the synthesized AiP-AgNPs mediated through the pneumatophore aqueous extract of *Acanthus ilicifolius*.

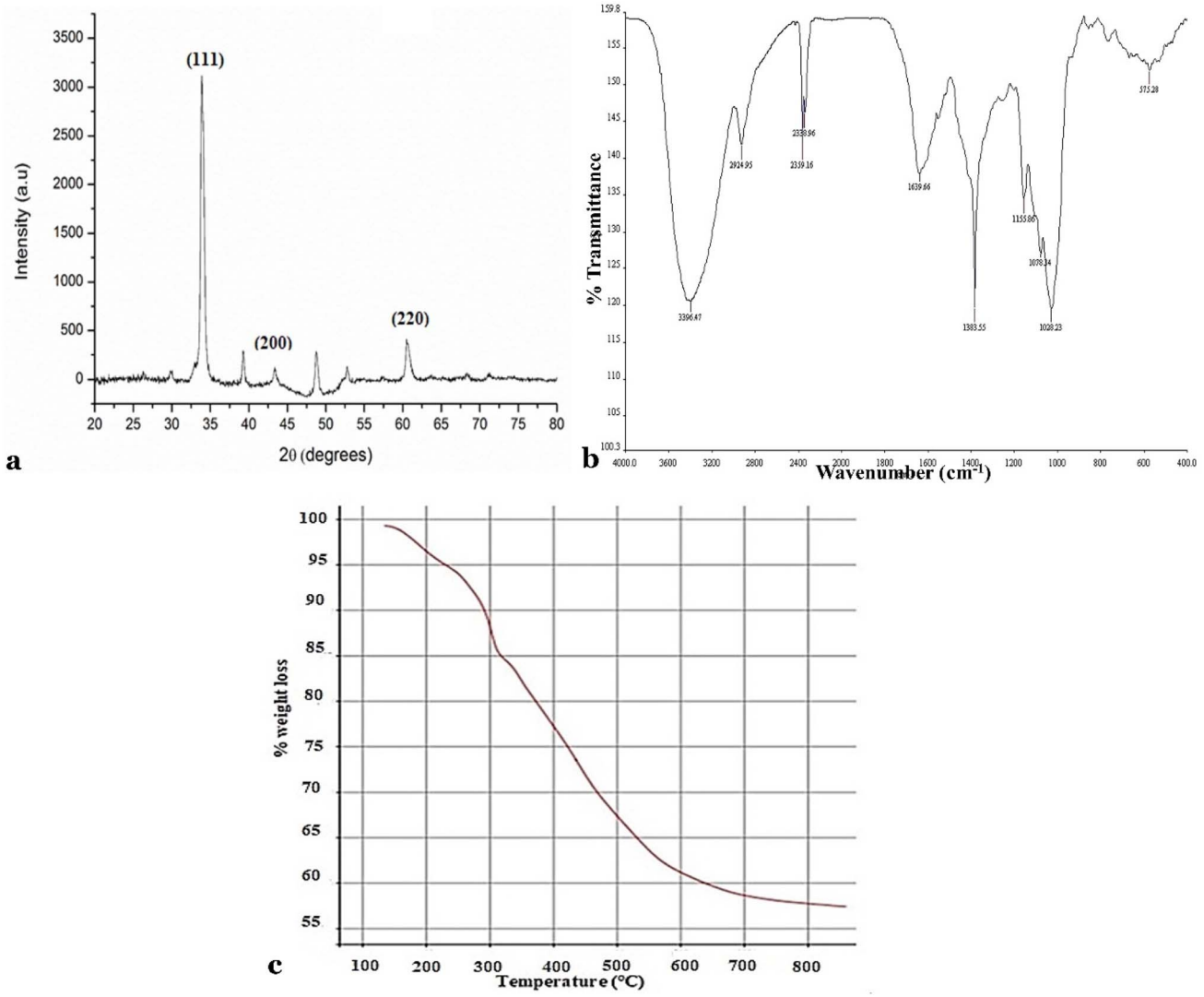

Fig. 6 Physio-chemical parameter screening of the synthesized AiP-AgNPs through (a) X-ray diffraction; (b) FTIR; and (c) thermo-gravimetric analysis.

Fig. 6a demonstrates the different crystalline lattices formed for the biologically synthesized AiP-AgNPs. The as-prepared nanoparticles exhibit lattice planes of (111), (200) and (220), respectively, which were again compared with the standard Joint Committee on Powder Diffraction Standards (JCPDS) database bearing file no. 04-0783. The average grain size of the synthesized AiP-AgNPs was calculated using Scherrer's formula,[49] indicating their crystalline size to be around ~25 nm. The results from the XRD studies collaborate with other physical characterization techniques of AFM, cryo-TEM, and FE-SEM analyses. FTIR spectroscopy is a spectroscopic technique that provides insights into the different vibrational frequencies of the bonds associated with the compounds in the examined material.[50] It is evident from Fig. 6b that different transmittance peaks correspond to the associated functional groups in the as-synthesized AiP-AgNPs. The characteristic wavenumbers ~ 3400 cm^{-1} and 2350 cm^{-1} correspond to –OH functional groups that signify the presence of phenolic groups. The other associated wavenumbers, such as 1630 cm^{-1} and 1340 cm^{-1}, correspond to the N–O stretching vibrations. The presence of different pharmaceutically active compounds, such as neopestalotin D; L-β-(3-hydroxyureido)-alanine; *N*-hexadecylethanolamine; semiplenamide F; erucamide; naphthacemycin C1; hemin; *N*-[5-(1,3-dithian-2-yl)-2-pentyn-1-yl]-3,4-dimethoxy-*N*-methylaniline; *N*-(sulfanylacetyl)-L-seryl-L-argininamide; myristyl sulphate and 3-[(13-methyltetradecyl)oxy]propyl hydrogen ({[(2*S*)-1-(4-amino-2-oxo-1(2*H*)-pyrimidinyl)-3-hydroxy-2-propanyl]oxy}methyl)phosphonate, as indicated through the LC-HRMS studies, might play a prominent role in the biological reduction of $AgNO_3$ salt to AiP-AgNPs.

Thermal Gravimetric Analysis (TGA) is an analytical technique in which the physical and chemical properties of the sample are measured with the changing temperature *versus* weight loss.[51] The technique works by increasing the temperature exposure to the sample, in return for which the volatile component present in the sample tends to become desorbed or

lost. This change in the weight loss properties is usually examined by TGA analyses, and the inherent temperature-interface physical and chemical properties of the samples are evaluated and measured. The different functional groups and associated compounds with the AiP-AgNPs seem to be desorbed in the temperature range of 200–700 °C with the corresponding % weight loss, as shown in Fig. 6c. It could be understood that, with the increase in the exposure temperature, there is a disentanglement in the stronger bonds in the structure of biogenic AgNPs. In the present investigation, AiP-AgNPs exhibit a pronounced change in the physical and chemical properties (200–700 °C), indicating the application under specific temperature conditions.

Reactive oxygen species (ROS) and antioxidants are naturally produced in the body owing to their metabolism, and both of them play important roles in the functioning of the body at the cellular level.[11] Thus, antioxidants help maintain a balance between oxidation and reduction reactions, thereby minimizing the long-term effects of ROS radicals.[52] In ayurveda, the diseased conditions were healed using various concoctions of

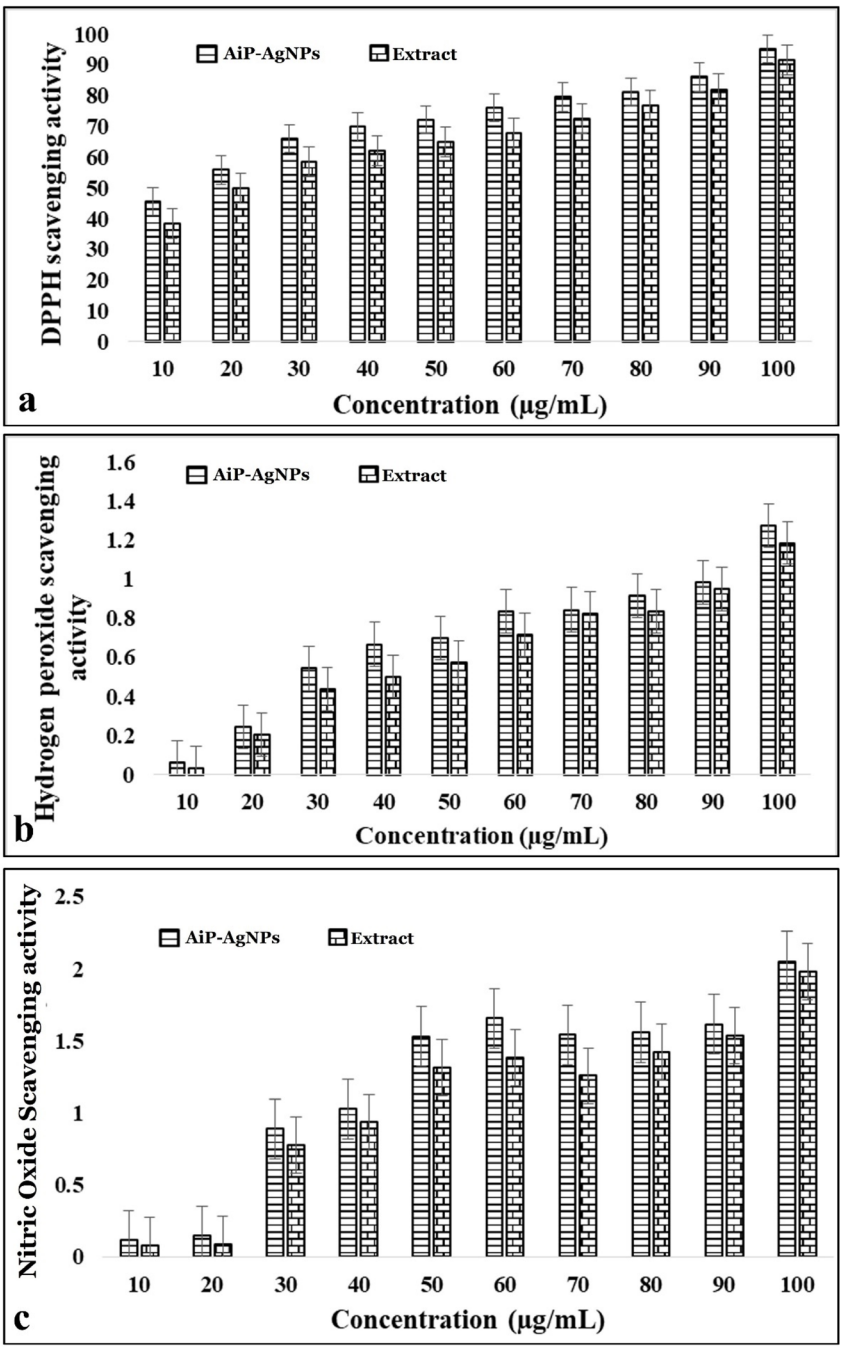

Fig. 7 Antioxidant activity screening of the synthesized AiP-AgNPs and pneumatophore aqueous extract through (a) DPPH radical scavenging assay; (b) hydrogen peroxide scavenging assay and (c) nitric oxide scavenging assay.

plant products; thus, the traditional knowledge of the locals was inspired by it. Hence, the synthesized AiP-AgNPs were screened owing to their antioxidant potential against some naturally occurring ROS in the body, such as nitric oxide and hydroxyl radicals. Fig. 7a illustrates that the DPPH radical scavenging activity of the synthesized AiP-AgNPs. 2,2-diphenyl-1-picrylhydrazyl (DPPH) is a standard antioxidant screening assay, in which the scavenging profile of the stable free radical DPPH is examined using test samples. The formation of hydrazine thus causes the change in color of the DPPH dye from violet to yellow color.[53] The synthesized AiP-AgNPs demonstrated dose-dependent DPPH radical scavenging activity, while the pneumatophore aqueous extract also exhibited a similar trend of DPPH radical scavenging at 100 μg mL^{-1} concentration.

Fig. 7b shows the hydrogen peroxide scavenging activity of the synthesized AiP-AgNPs. With the increase in concentration, the AgNPs demonstrated strong scavenging activity concerning the pneumatophore aqueous extract. Hydrogen peroxide (H_2O_2) is a very potent and powerful oxidizing agent that can activate the process of cellular differentiation and cellular proliferation through cell–cell signalling pathways.[54] During normal metabolism, H_2O_2 is generated *via* the activity of the cellular enzyme superoxide dismutase; however, accumulation of H_2O_2 in the cell leads to cellular damage, necrosis and apoptosis. The accumulated H_2O_2 eventually gets decomposed to the hydroxyl radical ($^{\bullet}OH$). The highly reactive hydroxyl radical sequentially leads to lipid peroxidation and subsequent tissue degeneration and ignites the pathological conditions associated with cancer, diabetes, and other inflammatory reactions.[55]

Fig. 7c demonstrates the nitric oxide scavenging potential of the as-synthesized AiP-AgNPs. Nitric oxide is a water-soluble gas that is commonly produced during the biological decay of organic matter. It has a very essential role in signal transduction and acts as a broad-spectrum antibiotic for the human body.[56] However, at even slightly higher nanomolar concentrations, it can inhibit essential citric acid cycle enzymes and respiratory enzymes. Further, by forming peroxynitrite, it can lead to potential tissue and other biomolecules, such as DNA and proteins.[57] Similar to the mechanism of hydrogen peroxide scavenging activity, the nitric oxide scavenging activity is based on the ability of the antioxidants to reduce the nitric radical species through the mechanism of lipid peroxidation and, subsequently, the overall cellular membrane, nuclear membrane, and mitochondrial membrane of the cells becomes damaged.

Evaluating the haemocompatibility of any designed nanoparticles and their interaction with the blood corpuscles is an important criterion in the pharmaceutical industry. Mostly, nanoparticles are designed for targeted delivery; hence, they encounter blood irrespective of their mode of administration. Therefore, the haemocompatibility of the synthesized AiP-

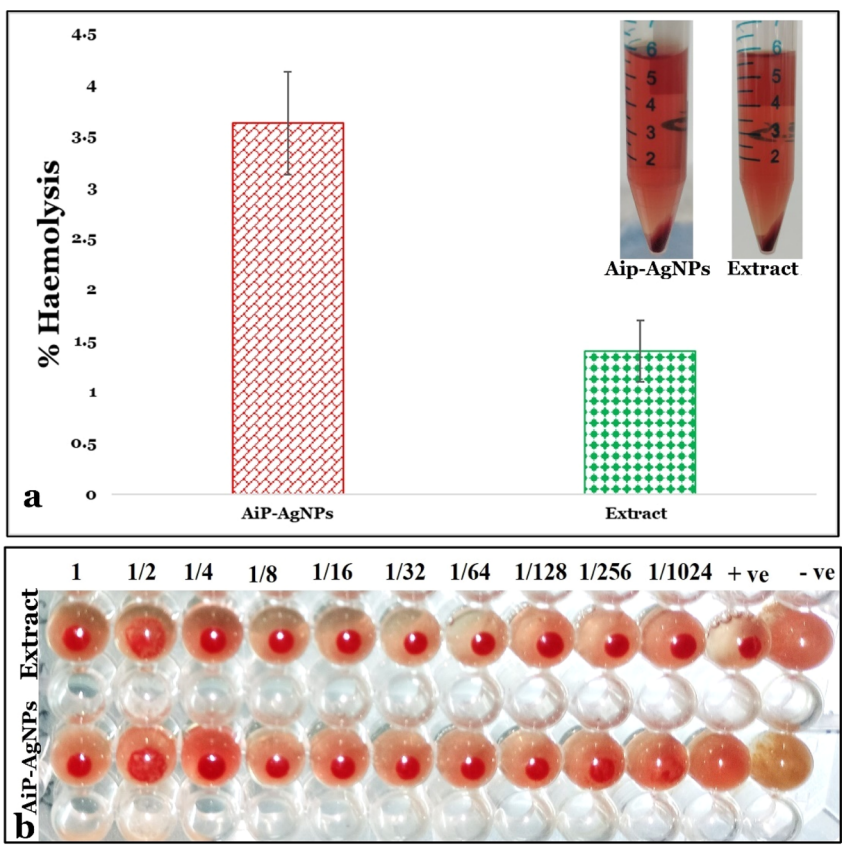

Fig. 8 Haemocompatibility activity screening of the synthesized AiP-AgNPs with the blood corpuscles through (a) haemolysis assay and (b) haemagglutination assay.

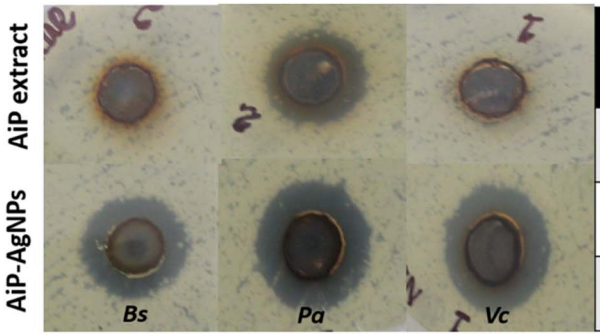

Microorganisms	AiP Extracts (in mm)	AiP-AgNPs (in mm)
Bacillus subtilis	0.00±00	09.83±0.23
Pseudomonas aeruginosa	8.16±0.62	15.33±0.47
Vibrio cholerae	0.00±00	12.00±0.00

Fig. 9 Antibacterial activity of pneumatophore aqueous extract and AiP-AgNPs against *B. subtilis* (Bs), *P. aeruginosa* (Pa), and *V. cholerae* (Vc).

AgNPs was tested using a haemolysis and haemagglutination assay. Fig. 8a shows the % haemolysis that occurred when the synthesized AiP-AgNPs were incubated with the red blood corpuscles. Both the test samples, *i.e.*, the synthesized AiP-AgNPs and the pneumatophore aqueous extract, exhibited negligible toxicity towards the RBCs. Similarly, Fig. 8b demonstrates that the haemagglutination activity of the synthesized AiP-AgNPs proved to be highly compatible, thereby forming an undisturbed globular structure at the bottom of the U-shaped 96 well plate. Similar results have been reported by our group for gold and silver nanoparticles synthesized using biological routes.[58,59] The size and morphology of the synthesized nanoparticles play a very pivotal role in providing the desired hemocompatibility. Thus, the design and synthesis of nanoparticles form an inevitable component for accessing their hemocompatibility and future therapeutic applications.

The antibacterial activity of the synthesized AiP-AgNPs and the pneumatophore aqueous extract of *Acanthus ilicifolius* were assessed using the agar well diffusion assay (Fig. 9). The agar-well method is highly effective and economical in assessing the antimicrobial activity of test agents against a wide range of pathogenic microorganisms.[60–62] In a recent antibacterial test, the AiP-AgNPs demonstrated significant activity against *P. aeruginosa*, with *V. cholera* and *B. subtilis* following suit, compared to the aqueous pneumatophore extract of *Acanthus ilicifolius*. Furthermore, the ability of *P. aeruginosa* to form biofilms, which can persist for extended periods and create a highly contagious environment in various industries or sectors, has gained

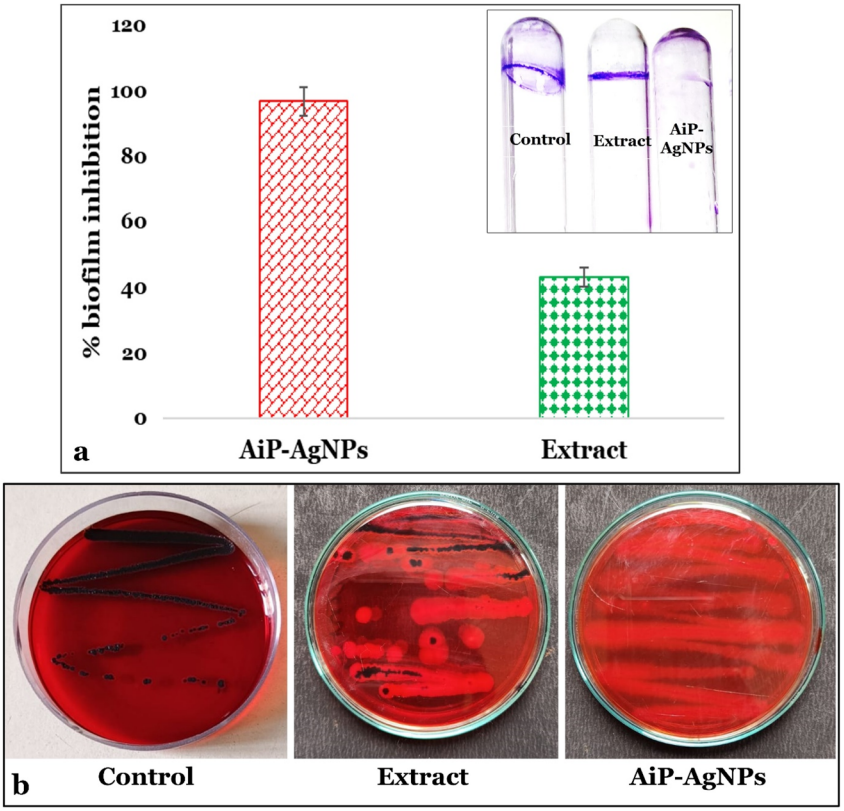

Fig. 10 Antibiofilm activity of the synthesized AiP-AgNPs against *Pseudomonas aeruginosa* through (a) tube assay and (b) Congo red assay.

widespread recognition. Based on the zone of inhibition results, it is evident that AiP-AgNPs can effectively eliminate *P. aeruginosa*. Our next step is to evaluate their effectiveness in preventing biofilm formation.

Biofilms are sessile colonies of bacterial communities that form strong film-like structures aided by their extracellular polymeric matrix substances (EPS). Thus, the EPS provides high resistance to antibiotics and antimicrobial compounds. Therefore, biofilm forms the main antagonist in food contamination illnesses and medical equipment-related infections in the healthcare industry.[63] Fig. 10a shows the biofilm-inhibiting activity of the synthesized AiP-AgNPs against the *P. aeruginosa* bacterial strain. The AiP-AgNP-treated test tube exhibiting a very thin crystal violet stained ring of biofilm formation concerning the untreated (control) test tube was observed visually. Further, to confirm the results of the tube assay, the Congo-red assay was performed. Fig. 10b illustrates the growth of bacterial colonies on Congo red agar plates, in which the formation of red and black colonies signifies their non-biofilm and biofilm-forming activity. The untreated control plate demonstrated the occurrence of dark black colonies, which confirms the formation of biofilm, while the AiP-AgNP-treated bacterial cells produced smooth red colonies on the Congo-red agar plate, further confirming the biofilm inhibiting activity of the biologically synthesized AiP-AgNPs from the pneumatophore aqueous extract of the mangrove plant *A. ilicifolius*.[64,65]

The cytotoxicity profile of the synthesized AiP-AgNPs against HepG2 hepatocarcinoma cells was screened using the MTT assay. MTT (3-(4,5-dimethylthiazol-2-yl)-2,5-diphenyltetrazolium bromide)tetrazolium dye is a very cost-effective and easy technique to screen the cytotoxicity profile of any designed and synthesized nanofabrication under *in vitro* conditions.[13] Fig. 11(i) depicts the dose-dependent cytotoxicity of the synthesized AiP-AgNPs against HepG2 hepatocarcinoma cells.

Fig. 11(ii) shows the effect of the synthesized AiP-AgNPs on HepG2 hepatocarcinoma cells analyzed through flow cytometry. Upon incubation, the hepatocarcinoma cells exhibited

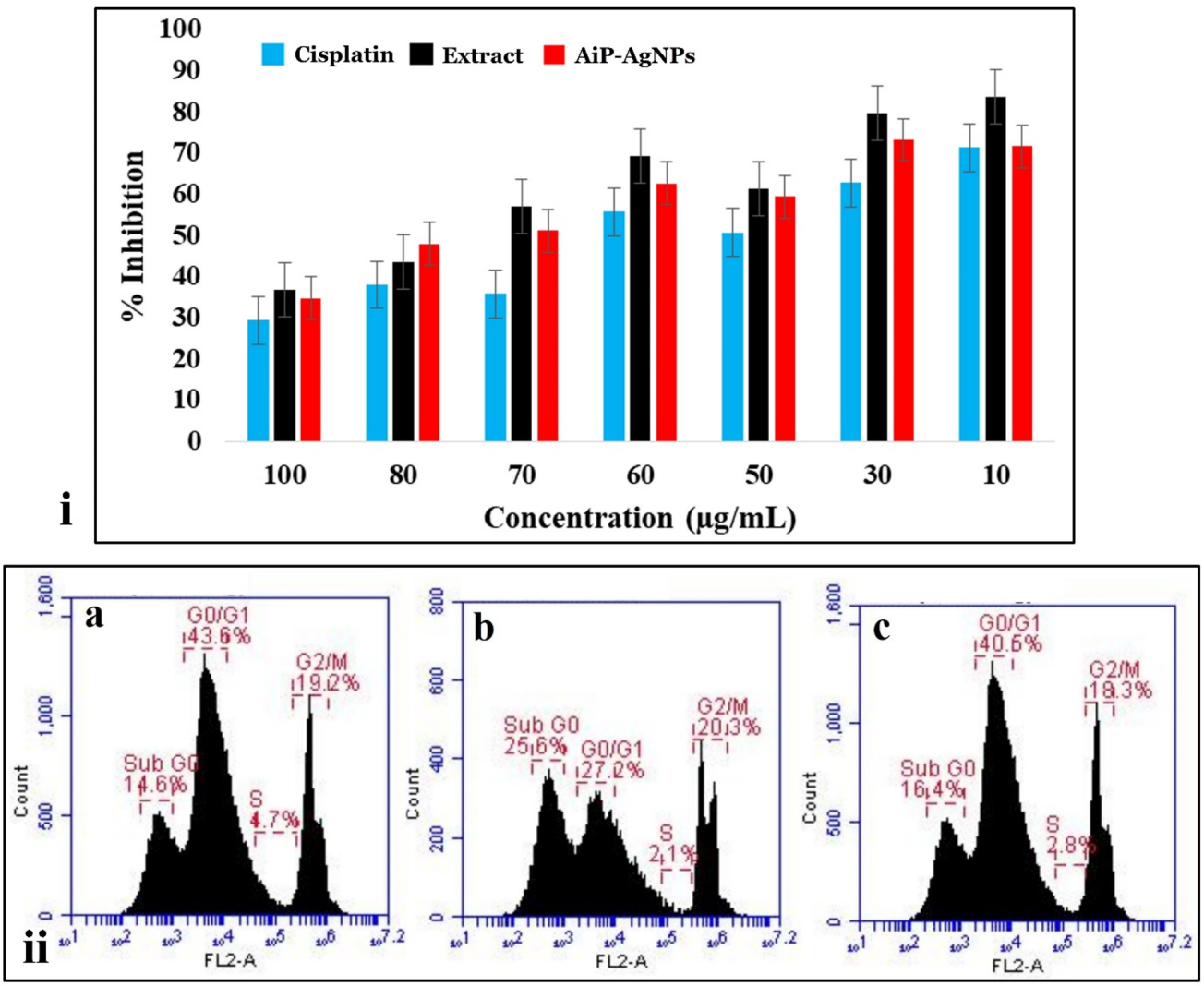

Fig. 11 Screening the cytotoxicity profile of the synthesized AiP-AgNPs through (i) MTT assay and (ii) cell cycle analysis through flow cytometry: (a) pneumatophore extract; (b) AiP-AgNPs and (c) standard anticancer drug cisplatin.

instability on the nucleolus and its contents, thereby arresting the cells to undergo mitotic cell division and condensing the chromatin and restricting the growth and synthesis phase of the cancerous cells. The occurrence of the sub-G_0 phase signifies the presence of apoptotic cells, which can indicate the cell death mechanism triggered by the synthesized AgNPs. The expression profile of G_2/M and the intensity of the S phase were highly hampered. The AiP-AgNP-treated HepG2 hepatic carcinoma cells exhibited 25.6% in the sub-G_0 phase, 27.2% in the G_0/G_1 phase, 2.1% in the S phase and 20.3% in the G_2/M phase. Similarly, the pneumatophore extract demonstrated 14.6% in the sub G_0 phase, 43.6% in the G_0/G_1 phase, 4.7% in the S-phase and 19.2% in the G_2/M phase. Thus, when compared with the MTT assay, it can be postulated that the synthesized AiP-AgNPs induced the arrest of synthesis and mitosis stages in the HepG2 cells along with their cellular destruction through apoptosis-mediated pathways. Similar reports have been described by Dziedzic's group, who postulated the possible role of Ag^+ ions released from the AgNPs encapsulated within the ethosomes; these ions interacted with the cellular components and arrested the cell cycle.[66]

The MTT and cell cycle analysis provided some insights into the possible role of the synthesized AiP-AgNPs in arresting the cellular growth and cell division of the HepG2 cells; therefore, the hepatocarcinoma cells were visualized under fluorescence microscopy for possible nuclear membrane damage through Hoechst staining. Fig. 12 demonstrates the potential role of the AiP-AgNPs in inducing nuclear membrane damage through Hoechst dye. Hoechst dye has a high affinity towards DNA and is impaired through intact plasma membrane; hence, when the nuclear membrane is compromised or damaged, the dye can easily bind with the DNA and give very high fluorescence intensity.[67] It is visible in Fig. 12b and c that upon treatment with the AiP-AgNPs and pneumatophore extract, the nuclear membrane is compromised, and the fluorescence intensity of the DNA molecule is very high when compared with the control untreated HepG2 cells. Similar results were reported on MG-63 osteosarcoma cells upon treatment with AgNPs synthesized using bark extracts of *Azadirachta indica* and *Ficus benghalensis*.[56]

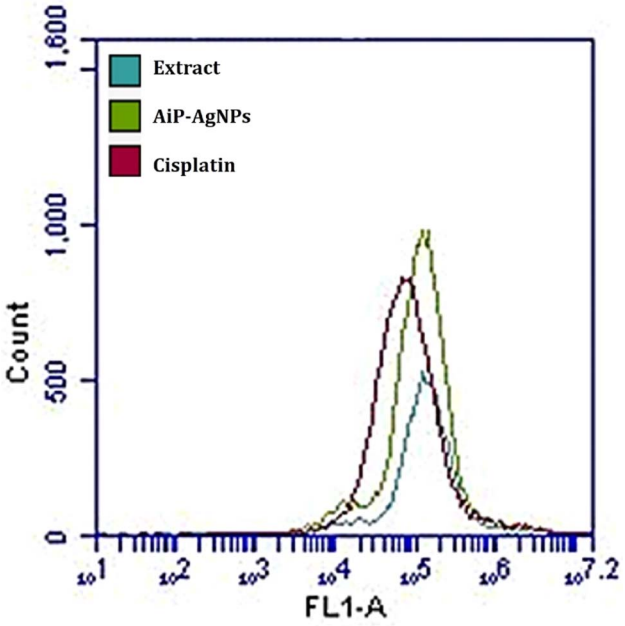

Fig. 13 Detection of intracellular ROS production using DCFH-DA dye *via* flow cytometry.

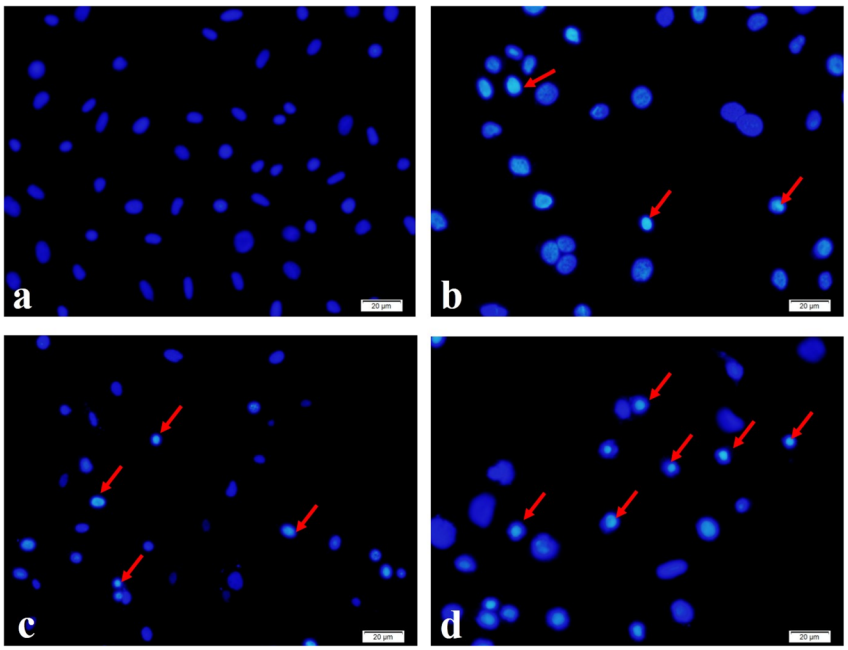

Fig. 12 Assessing the nuclear membrane damage using Hoechst 33342 stain in HepG2 cells and observed through epi-fluorescent microscope: (a) control group; (b) pneumatophore extract-treated group; (c) AiP-AgNP-treated group; and (d) cisplatin-treated group.

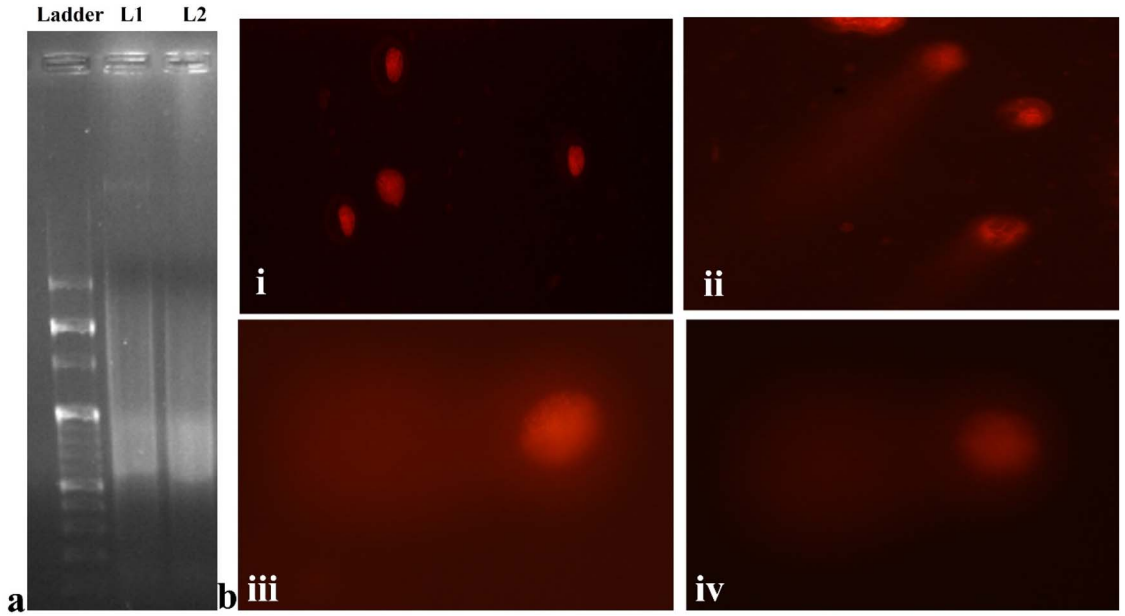

Fig. 14 Assessment of DNA damage of the HepG2 hepatocarcinoma cells upon treatment with AiP-AgNPs through (a) DNA fragmentation assay and (b) comet assay: (i) control; (ii) AiP-AgNP-treated cells; (iii) extract-treated cells; and (iv) standard cisplatin-treated cells.

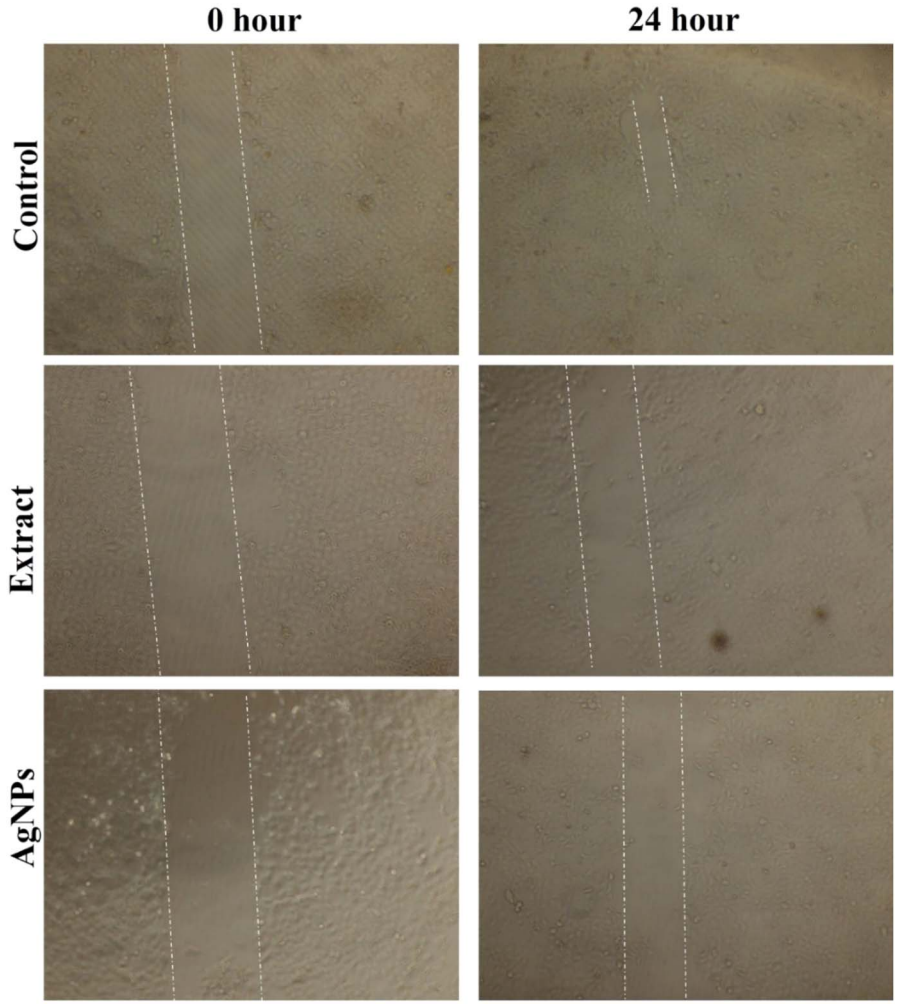

Fig. 15 Scratch wound healing activity of the synthesized AiP-AgNPs when treated against HepG2 hepatocarcinoma cells and observed through a light microscope.

From the results of the MTT assay, cell cycle analysis, and Hoechst staining, it was clear that the synthesized AiP-AgNPs could damage the cellular membrane of the HepG2 hepatocarcinoma cells. Hence, the internal ROS activity of the cancerous cells upon treatment with AiP-AgNPs was examined through 2′-7′-dichlorodihydrofluorescein diacetate (DCHF-DA) dye staining using flow cytometry (Fig. 13). Generally, as a result of normal metabolism, ROS are produced in the cell; however, increased ROS production leads to various pathophysiological conditions, such as cancer.[68] Conversely, these ROS radicals can also be used as a targeted weapon against cancerous cells, where the nanoparticles have been designed to induce excessive ROS production.[44] In the current investigation, the fluorescence activity of the AiP-AgNP cells was relatively higher when compared to the pneumatophore extract-treated cell group. These results concurred with our previously reported AgNPs synthesized using petal extracts of *Cucurbita maxima* against osteogenic Saos-2 cells.[69] Therefore, subsequent experiments were conducted to confirm the effects of these ROS radicals on the DNA machinery through DNA fragmentation assay and single-cell comet assay.

The fluorescence microscopy and flow cytometry analysis in HepG2 hepatocarcinoma cells upon treatment with the synthesized AiP-AgNPs exhibited chromatin condensation, with the inference of nuclear damage and excessive ROS production. Hence, the DNA damage analysis was conducted using agarose gel electrophoresis and a single-cell comet assay. Fig. 14a shows the DNA fragmentation upon incubation with the synthesized AiP-AgNPs and pneumatophore extract. It is well reported that in AgNPs and other metallic nanoparticle-treated DNA fragmentation assays, the DNAs of the cancerous cells are generally broken into small fragments, thereby developing a smear during agarose gel electrophoresis.[11,67] Fig. 14b shows a single-cell comet assay using fluorescence microscopy. When compared to the control and extract-treated cells, a long tail-like region is formed in the AiP-AgNP-treated cell groups when the DNA migrated inside the cell due to electrophoresis. The comet assay provides reliable information on the intensity of the DNA migration inside the cell as its nuclear envelope is compromised under the influence of ROS radicals produced by the synthesized nanoparticles.[70]

Metastasis is the signatory step of cancerous cells, where the cells, upon mutation, migrate from one place to another through the lymphatic or fluid connective tissue. Fig. 15 shows the scratch wound healing/migration assay of the HepG2 cells upon incubation with the synthesized AiP-AgNPs. From the scratch assay, it can be observed that compared to the size of the scratch initiated at the 0^{th} hour, it has not been filled up by the cancerous cells after 24 hours, signifying their potential to arrest the cells from migrating from one path to another. Similarly, the pneumatophore extract-treated cell group also demonstrated migration-arresting properties of the HepG2 cells compared to the control untreated cells. The results from the ROS production, DNA fragmentation and migration/scratch assay provide a strong insight into the potential efficacy demonstrated by the synthesized AiP-AgNPs against the HepG2 hepatocarcinoma cells. Similar results have been reported by Dash's group using ferromagnetic α-Fe_2O_3 NPs.[71]

4. Conclusion

The pneumatophores of the mangroves plants are the hidden treasury of bioactive compounds that have not been explored to their core potential. These compounds have not been investigated to the extent that they may be utilized to their full potential. The indigenous community in Odisha's coastal zone mostly uses pneumatophore extract to treat liver problems and snake bites of various kinds. The purpose of this study was to investigate the bioactive potential of pneumatophore extracts for the manufacture of silver nanoparticles (AgNPs) and determine their effectiveness against HepG2 hepatocellular cancer cells. The AgNPs that were made also had strong antibacterial, antibiofilm, and antioxidant effects against a strain of *P. aeruginosa* that formed biofilms. Further research, including preclinical and clinical evaluation, will unveil the untapped potential of AiP-AgNPs and position them as promising drug candidates. In addition, the study has a significant focus on the interaction of AiP-AgNPs against EPS and biofilm-forming genes, utilizing *in silico* and genomics approaches. This comprehensive study unveils the true potential of biogenic nanoparticles and their efficacy in delivering drugs against microorganisms and carcinoma cells.

Data availability

No consultancies were hired to write the manuscript, and no artificial intelligence software was used to write the manuscript. Data will be available upon request.

Author contributions

Conceptualization, D. N. and Y. K. M.; software, B. P. P.; validation and analysis, N. A. K., S. R., A. K. M. and Y. K. M.; resources, Y. K. M.; writing—original draft preparation, D. N., A. K. M., and K. B.; writing—review and editing, C. M., J. P., N. A. K., S. R. and Y. K. M.; characterization, C. M. and A. S.; data curation, D. N., A. K. M., K. B., N. A. K. and C. M.; supervision, D. N., B. P. P. and Y. K. M. All authors have read and agreed to the published version of the manuscript.

Conflicts of interest

The authors declare no conflict of interest.

Acknowledgements

The authors are highly indebted and extend their sincere thanks to SERB-DST, Government of India, for providing support to the Nano-biotechnology and Translational Knowledge Laboratory through Research Grant No. SRG/2022/000641 and Odisha State Higher Education Council, Odisha for providing support to Bioresources and Traditional Knowledge Laboratory through OURIIP-Seed Fund (17/Zoology-2020). Gujarat Biotechnology University is highly acknowledged for the LC/MS facility. The authors are also thankful to Siksha 'O' Anusandhan (Deemed to be University) for providing Open access funding.

References

1 R. Dhanker, T. Hussain, P. Tyagi, K. J. Singh and S. S. Kamble, *Front. Microbiol.*, 2021, **12**, 638003.
2 Q. Y. Tamboli, S. M. Patange, Y. K. Mohanta, A. D. Patil, R. Ali, I. Bushnak and K. Zakde, *ACS Omega*, 2024, **9**, 3835–3845.
3 H. Chopra, A. K. Mishra, I. Singh, Y. K. Mohanta, R. Sharma, T. Bin Emran and S. Bibi, *Int. J. Surg.*, 2022, **104**, 106713.
4 R. Sakthi Devi, A. Girigoswami, M. Siddharth and K. Girigoswami, *Appl. Biochem. Biotechnol.*, 2022, **194**, 4187–4219.
5 S. Ashe, D. Nayak, M. Kumari and B. Nayak, *ACS Appl. Mater. Interfaces*, 2016, **8**(44), 30005–30016.
6 D. Nayak, M. Kumari, S. Rajachandar, S. Ashe, N. C. Thathapudi and B. Nayak, *ACS Appl. Mater. Interfaces*, 2016, **8**(42), 28538–28553.
7 Y. K. Mohanta, A. K. Mishra, J. Panda, I. Chakrabartty, B. Sarma, S. K. Panda, H. Chopra, G. Zengin, M. G. Moloney and M. Sharifi-Rad, *Biochem. Biophys. Res. Commun.*, 2023, **688**, 149126.
8 W. H. Hunt, *Jom*, 2004, **56**, 13–18.
9 H. Barabadi, H. Noqani, F. Ashouri, A. Prasad, K. Jounaki, K. Mobaraki, Y. K. Mohanta and E. Mostafavi, *Talanta*, 2023, **256**, 124279.
10 D. Nayak, S. Pradhan, S. Ashe, P. R. Rauta and B. Nayak, *J. Colloid Interface Sci.*, 2015, **457**, 329–338.
11 D. Nayak, A. P. Minz, S. Ashe, P. R. Rauta, M. Kumari, P. Chopra and B. Nayak, *J. Colloid Interface Sci.*, 2016, **470**, 142–152.
12 Y. K. Mohanta, I. Chakrabartty, A. K. Mishra, H. Chopra, S. Mahanta, S. K. Avula, K. Patowary, R. Ahmed, B. Mishra, T. K. Mohanta, M. Saravanan and N. Sharma, *Front. Microbiol.*, 2022, **13**, 1028086.
13 T. Bhuyan, Y. K. Mohanta, K. Patowary, S. Maity, D. Nayak, K. Deka, K. Meenakshi Sundaram, S. Muthupandian and H. Sarma, *Curr. Res. Biotechnol.*, 2024, **7**, 100227.
14 S. Mitra, N. Naskar and P. Chaudhuri, *Phytomed. Plus*, 2021, **1**, 100107.
15 N. B. Sadeer, G. Zengin and M. F. Mahomoodally, *Crit. Rev. Biotechnol.*, 2023, **43**, 393–414.
16 A. Parthiban, R. Sivasankar, V. Sachithanandam, S. A. Khan, A. Jayshree, K. Murugan and R. Sridhar, *S. Afr. J. Bot.*, 2022, **149**, 899–915.
17 A. Parthiban, R. Sivasankar, V. Sachithanandam, S. A. Khan, A. Jayshree, K. Murugan and R. Sridhar, *S. Afr. J. Bot.*, 2022, **149**, 899–915.
18 S. C. Gnansounou, M. Toyi, K. V. Salako, D. O. Ahossou, T. J. D. Akpona, R. C. Gbedomon, A. E. Assogbadjo and R. G. Kakaï, *Trees, Forests and People*, 2021, **4**, 100080.
19 E. M. Awuku-Sowah, N. A. J. Graham and N. M. Watson, *Dialogues in Health*, 2022, **1**, 100059.
20 J. Umashankari, D. Inbakandan, T. T. Ajithkumar and T. Balasubramanian, *Aquat. Biosyst.*, 2012, **8**, 11.
21 C.-W. Lin, Y.-C. Kao, W.-J. Lin, C.-W. Ho and H.-J. Lin, *Forests*, 2021, **12**, 314.
22 H. Gajula, V. Kumar, P. D. Vijendra, J. Rajashekar, T. Sannabommaji and G. Basappa, in *Biotechnological Utilization of Mangrove Resources*, Elsevier, 2020, pp. 117–134.
23 S. Ghosh, M. Bakshi, S. Mahanty and P. Chaudhuri, *Water, Air, Soil Pollut.*, 2021, **232**, 1–21.
24 M. A. Varghese, A. M. Thomas and R. S. Kumar, *J. Mar. Biol. Assoc. India*, 2020, **62**, 74.
25 A. Parthiban, R. Sivasankar, V. Sachithanandam, S. A. Khan, A. Jayshree, K. Murugan and R. Sridhar, *S. Afr. J. Bot.*, 2022, **149**, 899–915.
26 M. H. Angio, E. Renjana, E. R. Firdiana and R. Irawanto, *Jurnal Penelitian Kehutanan Wallacea*, 2022, **11**, 53–70.
27 V. P. Sruthi, K. R. Sreenath, T. G. Sumithra, V. N. Anusree and P. S. Kurian, *J. Mar. Biol. Assoc. U. K.*, 2024, **104**, e41.
28 C. Pothiraj, P. Balaji, R. Shanthi, M. Gobinath, R. S. Babu, A. A.-D. Munirah, A. H. Ashraf, K. R. Kumar, V. Veeramanikandan and R. Arumugam, *J. Infect. Public Health*, 2021, **14**, 1927–1934.
29 N. G. Sarath, S. A. Manzil, S. Ali, A. A. Alsahli and J. T. Puthur, *PLoS One*, 2022, **17**, e0263753.
30 S. Aisiah, R. K. Rini, W. A. Tanod, F. Fatmawati, N. A. Fauzana, O. Olga and P. H. Riyadi, *J. Appl. Pharm. Sci.*, 2022, **12**, 57–69.
31 R. Patel, N. Patel, K. Patel, M. Patel, K. Patel, P. Verma and M. Shah, *WJPPS*, 2020, **9**, 471–489.
32 I. Khan, H. Rahman, N. M. Abd El-Salam, A. Tawab, A. Hussain, T. A. Khan, U. A. Khan, M. Qasim, M. Adnan, A. Azizullah, W. Murad, A. Jalal, N. Muhammad and R. Ullah, *BMC Compl. Alternative Med.*, 2017, **17**, 247.
33 S. Singh, K. Biswas, S. Chowdhury, Y. K. Mohanta and J. Bandyopadhyay, *Mater. Focus*, 2017, **6**, 1–8.
34 Y. K. Mohanta, K. Biswas, J. Bandyopadhyay, D. De, D. Mohanta, S. K. Panda, R. Jayabalan, T. K. Mohanta and A. K. Bastia, *Mater. Focus*, 2018, **7**, 1–6.
35 M. Sharifi-Rad, F. Epifano, S. Fiorito and J. M. Álvarez-Suarez, *Plants*, 2020, **9**(5), 646.
36 B. M. Ali, M. Boothapandi and A. Sultan Nasar, *Data Brief*, 2020, **28**, 104972.
37 Z. Guo and P. J. Sadler, *Angew. Chem., Int. Ed.*, 1999, **38**, 1512–1531.
38 D. Nayak, S. Ashe, P. R. Rauta and B. Nayak, *J. Appl. Biomed.*, 2017, **15**, 119–132.
39 S. Rana, A. Sen, S. Malla, M. Rai, P. Dash, B. Nayak and D. Nayak, *Geomicrobiol. J.*, 2023, **40**, 766–774.
40 N. Mangwani, S. Kumari and S. Das, *Biotechnol. Genet. Eng. Rev.*, 2016, **32**, 43–73.
41 S. Mori, A. Yamada and K. Kawai, *Jpn. J. Vet. Res.*, 2024, **71**, 109–116.
42 D. Sengupta, M. Deb, S. K. Rath, S. Kar, S. Parbin, N. Pradhan and S. K. Patra, *Exp. Cell Res.*, 2016, **346**, 176–187.
43 S. Kar, D. Sengupta, M. Deb, A. Shilpi, S. Parbin, S. K. Rath, N. Pradhan, M. Rakshit and S. K. Patra, *Clin. Epigenet.*, 2014, **6**, 1.
44 D. Nayak, N. C. Thathapudi, S. Ashe and B. Nayak, *Int. J. Pharm.*, 2021, **596**, 120265.

45 F. Atsushi, K. Yong-Pil, A. Matsumoto, Y. Takahashi, M. Suzuki, O. Hideyuki, H. Tomoda, M. Hidehito, H. Hideaki and I. Masato, *J. Antibiot.*, 2017, **70**, 562–567.
46 D. Nayak, S. Pradhan, S. Ashe, P. R. Rauta and B. Nayak, *J. Colloid Interface Sci.*, 2015, **457**, 329–338.
47 D. Nayak, S. Ashe, P. R. Rauta and B. Nayak, *IET Nanobiotechnol.*, 2015, **9**, 288–293.
48 Y. K. Mohanta, D. Nayak, K. Biswas, S. K. Singdevsachan, E. F. Abd_Allah, A. Hashem, A. A. Alqarawi, D. Yadav and T. K. Mohanta, *Molecules*, 2018, **23**, 655.
49 D. Nayak, A. Boxi, S. Ashe, N. C. Thathapudi and B. Nayak, *Mater. Sci. Eng., C*, 2017, **73**, 406–416.
50 A. Prasad, A. Khatua, Y. K. Mohanta, M. Saravanan, R. Meena and I. Ghosh, *Nanoscale*, 2022, **14**, 10399–10417.
51 K. Biswas, Y. Kishore, M. Awdhesh and K. Mishra, *J. Mater. Sci.: Mater. Med.*, 2021, **32**, 151.
52 S. Ashe, D. Nayak, M. Kumari and B. Nayak, *ACS Appl. Mater. Interfaces*, 2016, **8**, 30005–30016.
53 B. Holst and G. Williamson, *Curr. Opin. Biotechnol.*, 2008, **19**, 73–82.
54 J. M. Matés and F. M. Sánchez-Jiménez, *Int. J. Biochem. Cell Biol.*, 2000, **32**, 157–170.
55 F. Shahidi, In *Phenolics in Food and Nutraceuticals*, 2003.
56 D. Nayak, S. Ashe, P. R. Rauta, M. Kumari and B. Nayak, *Mater. Sci. Eng., C*, 2016, **58**, 44–52.
57 J. S. Duhan, R. Kumar, N. Kumar, P. Kaur, K. Nehra and S. Duhan, *Biotechnol. Rep.*, 2017, **15**, 11–23.
58 Y. K. Mohanta, K. Biswas, A. K. Mishra, B. Patra, B. Mishra, J. Panda, S. K. Avula, R. S. Varma, B. P. Panda and D. Nayak, *RSC Adv.*, 2024, **14**, 27816–27830.
59 D. Nayak, A. K. Mishra, S. Malla, U. Swain, K. Panigrahi, J. Panda, S. Rustagi, P. R. Rauta and Y. K. Mohanta, *ECS J. Solid State Sci. Technol.*, 2024, **13**, 87003.
60 L. Prabakaran, W. V. Sathyaraj, B. V. Yesudhason, G. K. Subbaraj and R. Atchudan, *Chemosensors*, 2023, **11**(7), 373.
61 K. Monisha, S. Antinate Shilpa, B. Anandan and G. S. Hikku, *Eng. Res. Express*, 2023, **5**, 25054.
62 K. Rameshkumar, V. Ananthi, A. Arun, P. Prema, V. Veeramanikandan, V.-H. Nguyen and P. Balaji, *Mater. Today Commun.*, 2023, **35**, 105980.
63 S. Rana, A. Sen, S. Malla, M. Rai, P. Dash, B. Nayak and D. Nayak, *Geomicrobiol. J.*, 2023, **40**, 766–774.
64 A. Basnet, B. Tamang, M. R. Shrestha, L. B. Shrestha, J. R. Rai, R. Maharjan, S. Dahal, P. Shrestha and S. K. Rai, *PLoS One*, 2023, **18**, e0294646.
65 V. L. P. Sri, S. Srinivasan, S. Muthukumar, S. Chellaswamy, N. N. Nachiappan and S. Thamilselvan, *J. Oral Maxillofac. Pathol.*, 2023, **27**, 693–699.
66 A. Dziedzic, R. Kubina, J. R. Bułdak, M. Skonieczna and K. Cholewa, *Molecules*, 2016, **21**(3), 365.
67 D. Nayak, S. Ashe, P. R. Rauta and B. Nayak, *J. Appl. Biomed.*, 2017, **15**(2), 119–132.
68 H. Wiseman and B. Halliwell, *Biochem. J.*, 1996, **313**(pt 1), 17–29.
69 S. Ashe, D. Nayak, M. Kumari and B. Nayak, *ACS Appl. Mater. Interfaces*, 2016, 6b10639, acsami.
70 J. Shah, S. Bhagat and S. Singh, in *Nanotoxicity: Prevention and Antibacterial Applications of Nanomaterials*, 2020.
71 P. Dash, S. Pattanayak, M. majhi and B. Nayak, *J. Alloys Compd.*, 2023, **957**, 170383.